International Journal of Plasticity 136 (2021) 102854

Contents lists available at ScienceDirect

International Journal of Plasticity

journal homepage: www.elsevier.com/locate/ijplas

The influence of nano/micro sample size on the strain-rate sensitivity of plastic flow in tungsten

Pratyush Srivastava [a], Katherine Jiang [b], Yinan Cui [c,a,*], Edgar Olivera [b], Nasr Ghoniem [a,b], Vijay Gupta [a,b]

[a] Mechanical and Aerospace Engineering, University of California Los Angeles, Los Angeles, CA 90095, USA
[b] Materials Science and Engineering, University of California Los Angeles, Los Angeles, CA 90095, USA
[c] Applied Mechanics Lab., School of Aerospace Engineering, Tsinghua University, Beijing 100084, China

ARTICLE INFO

Keywords:
BCC crystal
Strain rate
Flow stress
Strain hardening
Dislocation avalanche

ABSTRACT

The plastic flow characteristics of body centered cubic metals, which is dominated by the motion of screw dislocations, generally exhibits strong strain rate dependence. In-situ scanning electron microscopy compression tests are performed on tungsten (W) single crystal nano and micro pillars, with diameters in the range 100–2000 nm. We demonstrate here that by reducing sample size, the strain rate sensitivity of plastic flow, including not only the yield strength but also the strain burst statistics, is reduced. It is found that the strain rate sensitivity of the flow stress scales with the sample size d as $d^{0.67}$. Statistical analysis of the strain burst size displays truncated power law scaling with a lower exponent at higher strain rate for micron size pillars. Nano size pillars (<500 nm) show near universal scaling exponent of 1.50 ± 0.07 at all applied strain rates. The strain hardening rate and deformation morphology are found not to be very sensitive to the strain rate. This external pillar sample size effect is further compared with the internal grain size in nanocrystalline W in order to guide the design of new materials by tuning the characteristic length scale (external or grain size)

1. Introduction

Tungsten (W) has long been of great technical interest because of its high melting point, low sputtering rate, good corrosion resistance, and high strength at high-temperatures. It is widely used in high-temperature and radiation-shielding applications, such as light bulbs, cathode-ray tube, plasma-facing components and rocket engine nozzles. In many applications and during long-term service, the strain rate can range from the typical creep strain rate ($\approx 10^{-6}$ s^{-1}) to very high strain rates ($\approx 10^{6}$ s^{-1}). As a typical body centered cubic (BCC) metal, the plastic flow behavior of W generally exhibits strong strain rate sensitivity (Dümmer et al., 1998; Gröger et al., 2008; El Ters and Shehadeh, 2019). Thus, the influence of the strain rate on plastic flow characteristics is also an important factor in the design of W components.

The strain rate sensitivity of W is associated with the motion of screw dislocations, because their non-planar core structure leads to very slow mobility, as compared to edge dislocations (Kim et al., 2010; Cereceda et al., 2016; Butler et al., 2018; Shinzato et al., 2019). Our recent work demonstrates that the role of screw dislocations in controlling plastic flow in bcc metals can be tuned by changing the external sample size (Cui et al., 2016a). At small scales, it is easy for screw dislocations to glide out of a free surface, which can drastically reduce stored screw dislocations. Thus, the mix of stored edge and screw dislocations can be controlled by

* Corresponding author at: Applied Mechanics Lab., School of Aerospace Engineering, Tsinghua University, Beijing 100084, China.
E-mail address: cyn@mail.tsinghua.edu.cn (Y. Cui).

https://doi.org/10.1016/j.ijplas.2020.102854
Received 18 November 2019; Received in revised form 2 September 2020
Available online 8 September 2020

changing sample size, in direct contrast to the traditional notion of a dislocation microstructure dominated by screw dislocations in bcc metals. In addition, the high flow stress due to the size effect helps screw dislocations to overcome the high Peierls stress. This finding of size dependent screw dislocation behavior leads to the hypothesis that the strain rate sensitivity in W may also be size-dependent. This implies that even though we may not be able to change the strain rate that a W component is subjected to in service, we can design the component with a characteristic length that renders it more resilient.

This hypothesis is to some extent supported by recent experimental results. For example, recent compression tests on bcc Fe pillars shows that the strain rate sensitivity of the yield stress decreases with the reduction of sample size (Huang et al., 2015). The strain rate sensitivity parameter (m) of bcc metals has also been reported to decrease with decreasing grain size, especially in nanocrystalline metals. Wei et al. (2006a) observed that the strain rate sensitivity of ultra-fine grained W is reduced to half the value of the large grain size W. Wang and Ma (2004) observed a decrease in the value of m from 0.04 for conventional Fe to 0.004 when the grain size of ultrafine-grained Fe was reduced to 80 nm. Cheng et al. (2013) reported similar behavior with nanocrystalline grain size for bcc Mo. They attributed this behavior to an increase in the density of mixed and edge dislocations, and the decrease in the density of screw dislocations with decreasing grain size, thereby reducing the strain rate sensitivity. This explanation is consistent with our recent findings of dislocation dynamics simulations on W single crystal nano pillars (Cui et al., 2016b).

One might then wonder whether a similar trend is also observed in nano and micro scale W samples. It is interesting to contemplate if there is a critical size for the strain rate insensitivity of the yield strength. Furthermore, going beyond the yield strength, the influence of size on the strain rate dependence of other plastic flow characteristics needs to be clarified (Cao and Koslowski, 2015; Cereceda et al., 2016; Xu et al., 2018). Firstly, strain hardening is usually a desirable behavior to avoid plastic instabilities. At small scales, there is currently a wide-ranging debate as to whether strain hardening is present for submicron single crystals under uniaxial compression. The experimental observations are summarized in Table 1 in Cui et al. (2014) for face centered cubic (fcc) crystals and listed in Table 1 for bcc crystals. The combined effect of size and strain rate on the strain hardening behavior is unclear yet (Voyiadjis and Song, 2019; Chen et al., 2018), and quantitative data is still missing. Secondly, the stress–strain curve at the sub-micron scale is not smooth and exhibits significant intermittency at small scales (Miguel et al., 2001; Zaiser, 2006; Ng and Ngan, 2008; Papanikolaou et al., 2017a; Maass and Derlet, 2018; Papanikolaou et al., 2017b; Jiang et al., 2019; Ni et al., 2019). Strain bursts and dislocation avalanches are widely observed at the nano- and micro-scales, and the underlying physics attract significant attention. Their statistics is found to be analogous to other non-equilibrium physical systems of vastly different spatial and temporal scales, implying the universality of the underlying physics (Sethna et al., 2001). The burst statistics of micron size BCC Mo pillar (Zaiser et al., 2008), fcc Au (Brinckmann et al., 2008), and Nb pillars (Sparks and Maass, 2018) compressed at lower strain rates (10^{-3} s^{-1}) are found to follow a universal power law scaling behavior. However, it has been reported that this universal behavior is not invariant under an applied strain rate. The strain-rate effects of cross-slip-driven relaxation phenomena were first proposed and simulated in coarse-grained continuum dislocation density models by Papanikolaou et al. (2012), and then more detailed simulations showed consistent effects in (Papanikolaou et al., 2017b; Song et al., 2019). The combined strain-rate and dislocation density effect on the burst statistics was thoroughly studied using two-dimensional discrete-dislocation dynamics (DDD) simulation (Papanikolaou et al., 2017b; Song et al., 2019; Song and Papanikolaou, 2019). The power law exponent is found to be influenced by the dislocation density, while different dislocation densities are expected under different applied strain rates. Recent compression tests on 2 μm Nb pillars demonstrate that the applied strain rate has a significant influence on both the burst frequency and burst size statistics, and can even lead to the intermittent-to-smooth transition of plastic flow (Sparks and Maaß, 2018; Sparks et al., 2019). If by going smaller in size, we can reduce the strain rate dependence of yield stress, then it might be possible to observe similar trend for burst statistics. Namely, it may be possible to observe strain rate insensitivity of the burst statistics when the external size is small enough. Then, one may ask if the critical size for the strain rate insensitivity is the same as that for the yield stress.

The present work aims to answer these questions, and for the first time attempts to give a complete picture of the influence of sample size on the strain rate dependence of plastic flow in W. This includes the yield strength, the strain hardening rate, strain bursts, and dislocation avalanches. The paper is organized as follows. In Section 2, the experimental set up is described. Size tuned strain rate sensitivity of the yield strength and strain hardening behavior is addressed in Section 3, followed with a discussion of the spatio-temporal intermittent plasticity in Section 4. We then highlight the concerns surrounding FIB micromachining technique in section 5. The competitive role of size and strain rate is discussed in Section 6. Concluding remarks are finally given in Section 7.

2. Experimental setup

Cylindrical micro and nano pillars of diameters ranging from 100–2000 nm were milled out of polished (100) W single crystal (9 mm diameter and 10 mm thick), purchased from Goodfellow Corporation. Pillars were made using the Focused Ion Beam (FIB) method with a gallium ion source operating at 30 kV, keeping the pillars axis along the [001]-orientation. The sample was first polished using 600 grit and 1200 grit silicon carbide abrasive disks until they became smooth to the naked eye. Then, they underwent a final polish using 1 μm α-alumina powder. The local roughness of polished W surfaces is insensitive to alumina particle size (Bielmann et al., 1999). According to the SEM observation, the local surface roughness is far smaller than the compression scale. Care was taken for locations of pillars to avoid any visible surface defects in the SEM. Using FEI Nova 600 DualBeam (FIB/SEM), pillars were made in 3 - 4 steps to minimize the taper and beam damage, as shown in Fig. 1. The multiple-step pillar milling procedure began with creation of the base well and viewing window for clearance and line of sight while performing in-situ compression. This first step was carried out at currents ranging from 0.5 nA to 5 nA, depending on the pillar diameter. The following steps to shape the pillar were performed at lower currents to reduce ion beam damage to the pillar. A final cleaning step to reduce taper was

Table 1
Strain hardening (SH) data from uniaxial compression experiments on bcc single crystal micro and nanopillars. Here, ε represents strain value, T represents temperature.

Material	Crystal orientation	Diameter d (μm)	Strain hardening
Mo (Brinckmann et al., 2008)	[001]	0.20–0.98	Decrease with reducing d
Mo (Huang et al., 2011)	[111]	0.20–1.20	Similar for different d
Mo, Ta (Schneider et al., 2009)	[001]	0.20–1.00	Presence when $\varepsilon < 5\%$, absence for large ε.
Ta (Abad et al., 2016)	[111]	0.50–5.00	Ta has weak SH at 25 °C, more significant SH for $d = 0.5$ μm at 200 °C
W (Abad et al., 2016)	[100]	0.50–5.00	Weak SH for $d = 5.0$ μm, relatively larger SH for $d = 0.5$ μm
W (Schneider et al., 2009)	[001]	0.20–5.00	Absence when $\varepsilon < 4\%$, presence for larger ε
Nb (Schneider et al., 2009)	[001]	0.20–5.00	More significant SH for $d = 0.2$ μm
Nb (Kim et al., 2009)	[001]	0.20–0.90	More significant SH for tension than compression
Fe, Nb, and V (Yilmaz et al., 2019)	[001]	0.20–5.00	Increase with decreasing d, at 23 °C and −80 °C
Fe (Hagen et al., 2017)	[010], [011]	1.00	Increase with decreasing temperature

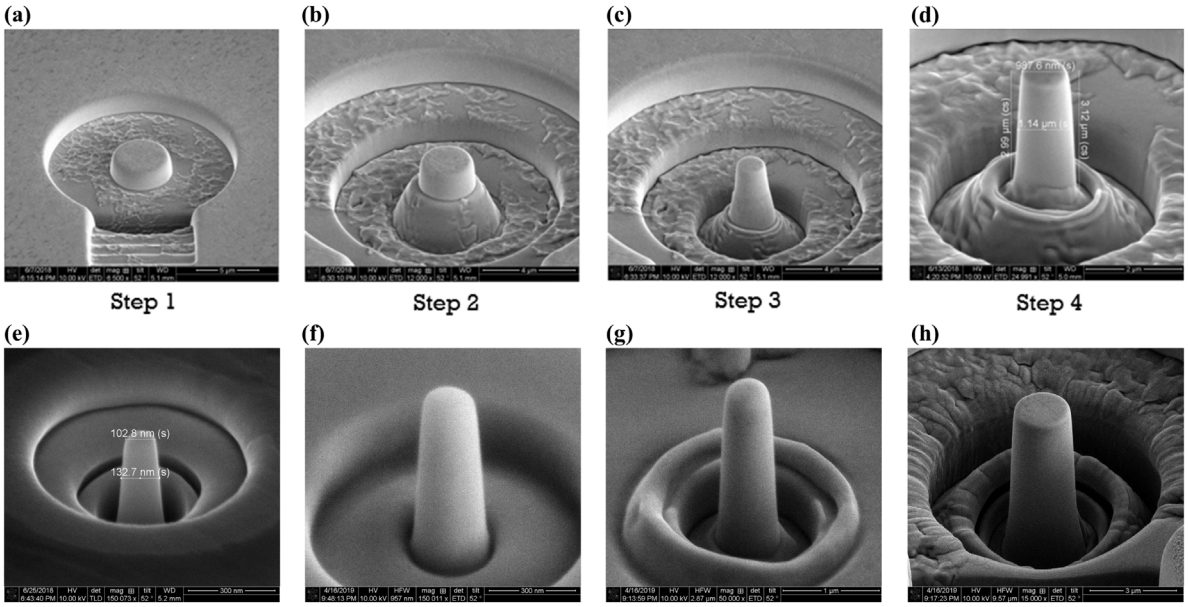

Fig. 1. (a), (b), (c), and (d) are the SEM pictures of milling steps of a representative 1000 nm W pillar using a 4-step *in-situ* SEM FIB method. (e), (f), (g), and (h) are the SEM pictures of representative 100, 200, 500, and 2000 nm pillars respectively.

implemented at extremely low currents after all intermediate diameter-decreasing steps were completed, ranging from 1 pA for the smallest (100 nm) pillars to 100 pA for the micron sized pillars. The final milling step at pA level ion currents also helps in reducing the ion-beam damaged layer from the pillar surface. For pillars of diameters 500, 1000, and 2000 nm, the aspect ratio (length/diameter) was kept around 3. However, for smaller pillars of diameter 100 and 200 nm, this ratio was around 5 because of the difficulty in minimizing the side-wall taper. The taper in the pillars was $2.0 \pm 0.5°$ for 2000 nm and 1000 nm diameter, $2.5 \pm 0.5°$ for 500 nm, and $3.5 \pm 0.75°$ for 200 and 100 nm diameters. The pillar taper in this work is similar to almost all other micropillar studies using FIB manufacturing technique (Frick et al., 2008; Volkert et al., 2006; Greer and De Hosson, 2011). Errors in the stress and strain as large as several percent can be expected due to ignoring column taper, rounding at the top and bottom of the column, and nonplanarity and friction between the diamond punch and column top (Zhang et al., 2006, 2014; Volkert et al., 2006). Some aspects of the FIB induced complication will be further discussed in Section 5.

The uniaxial compression tests were performed using the Hysitron PI 85L PicoIndenter, equipped with a flat punch tip of 5 μm in diameter, inside FEI Nova 600 DualBeam (FIB/SEM). A displacement-controlled loading mode was selected for all experiments and the loading rates were chosen to achieve an applied strain rate range from 10^{-3} s^{-1} to 10^{-1} s^{-1}. The data acquisition rate was selected for each experiment based on the compression speed. Load displacement data obtained from the PicoIndenter software was converted to stress–strain plots using the measured lengths and diameters. The diameter was measured at the middle pillar section

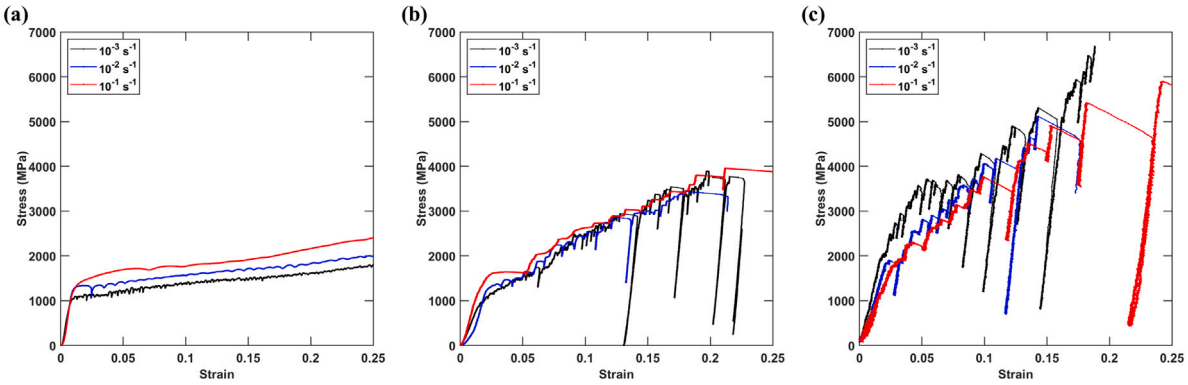

Fig. 2. Typical engineering stress–strain curves of W pillars with diameters (a) 2000, (b) 500 and (c) 100 nm tested at different applied displacement rate of the compressor tip corresponding to strain rates of $10^{-3}, 10^{-2}$ and 10^{-1} s^{-1}.

due to its tapered shape. In previous work, the maximum strain value in experiments is generally less than 20% (Schneider et al., 2009; Abad et al., 2016). In the current work, compressions were performed for a wide range of strain values (20% to 50%) to give more complete information. For each size at each strain rate, 7–10 tests were carried out.

3. Size tuned strain rate sensitivity of flow stress

The stress–strain curves are shown in Fig. 2 for representative pillars at different strain rates. It clearly demonstrates that with the reduction of the sample size, the strain rate dependence changes significantly. For 2000 nm pillar, the stress–strain curves exhibit obvious strain rate effects (see Fig. 2a). When the pillar diameter decreases to 500 nm, the flows stress seems to be strain rate insensitive (see Fig. 2b).

In the following subsections, the size-tuned strain rate sensitivity of the yield stress and strain hardening rate are further quantitatively analyzed.

3.1. Strain rate sensitivity of the yield strength

The yield strength of the bulk material is usually estimated as the stress value taken at 0.2% offset strain. With respect to the experimental tests at the micro and nano scale, the yield strength is generally measured at a strain value between 2% and 10% (Uchic et al., 2009), to avoid the effects of initial microplasticity, misalignment, and the rounding of the tip especially in smaller diameter pillars (Byer and Ramesh, 2013). Accordingly, the stress at 8% strain is treated as the yield strength σ_y (flow stress) in this work. The yield strength data was then fitted as a function of the strain rate as, $\sigma_y = A\dot{\epsilon}^m$, where A is the fitting constant, and $\dot{\epsilon}$ is the applied strain rate. The strain rate sensitivity parameter m for the yield strength is given as,

$$m = \frac{\partial(\ln \sigma_y)}{\partial(\ln \dot{\epsilon})} \tag{1}$$

Fig. 3(a) gives the yield strength as a function of the strain rate in a log–log plot. The strain rate sensitivity parameter m is obtained by fitting the slope of the corresponding data. As expected, m decreases gradually from 0.050 to 0.011 when the pillar size is decreased from 2000 to 200 nm. The 100 nm pillar shows a negative value of m (= −0.017). The low absolute value of this calculated negative strain rate sensitivity parameter is negligible compared to the typical scatter observed for such small pillar tests. For example, the large burst events in 100 nm, as evident in Fig. 2c, lead to higher scattering in the flow stress values obtained at 8% strain, compared to larger sized pillars. Therefore, the yield strength of 100 nm pillars can be considered as strain rate insensitive, and m is close to 0. This size dependent strain rate sensitivity trend shown in Fig. 3(a) is consistent with other observations for Fe, where Huang et al. (2015) reported a decrease in the value of m from 0.0628 to 0.0055, with a decrease in diameter from 1000 nm to 200 nm, as shown in Fig. 3b. Similar weak or no strain rate sensitivity of yield stress at submicron and micron scales is also observed in other BCC pillars (Chen et al., 2018; Schneider et al., 2011; Pozuelo et al., 2019). A reduced m value with the decrease in sample size is also widely observed in nano-crystals (Wei et al., 2004), as summarized in Section 3.

On the other hand, the competition between the size and strain rate effects on the yield strength can also be interpreted through the strain rate dependence of the size. Based on this consideration, we alternatively plot the yield strength as a function of size at different strain rates. It is found from Fig. 4 that with the reduction of the sample size, the yield strengths at different strain rates start to overlap and then change their trend, due to a transition from a positive strain rate dependence to a negative one. Fig. 4 suggests that the size effect is more significant at lower strain rates. Quantitatively, the size effect is described by,

$$\sigma_y = \sigma_0 + kd^{-\alpha} \tag{2}$$

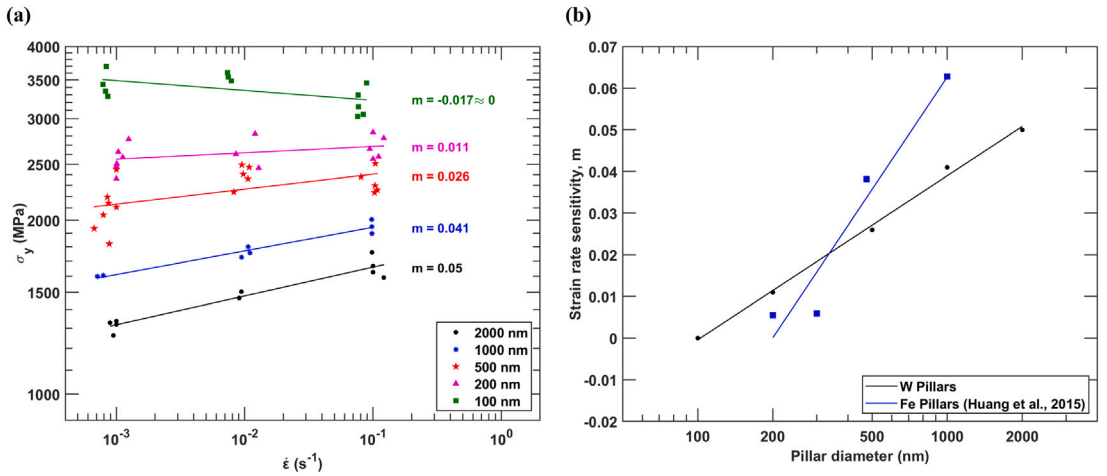

Fig. 3. Strain rate and size dependence of the flow stress (at 8% strain), σ_y for W pillars. (a) Double logarithmic plot of flow stress, σ_y vs. strain rate $\dot{\epsilon}$ at different pillar diameters with the strain rate sensitivity parameter, m as the slope of the linear fit. (b) Semi logarithmic plot of the strain rate sensitivity parameter, m vs. pillar diameter for W pillars and Fe pillars (taken from literature).

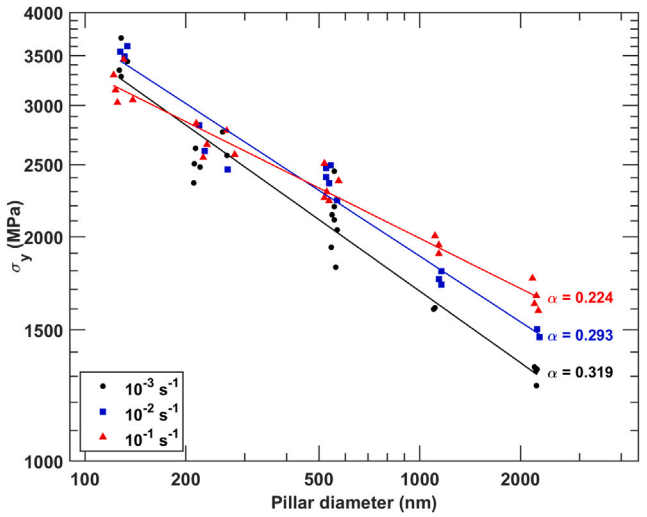

Fig. 4. Double logarithmic plot of the flow stress, σ_y vs. pillar diameter at different strain rates with size effect power law exponent, α as the slope of the linear fit.

where σ_0 is the bulk strength of the material,[1] d is the characteristic length scale, k is a constant, and α is the power law exponent. As shown in Fig. 4, the power law exponent, α decreases from 0.319 to 0.224 with an increase in the strain rate from 10^{-3} s^{-1} to 10^{-1} s^{-1}. This data is consistent with the one presented by Abad et al. (2016), which shows a power law exponent of 0.33 at 25 °C and 10^{-3} s^{-1} strain rate for (100) W, using flow stress values at 2.5% strain. Kim et al. (2010) report 0.44(±0.11) power law exponent for flow stress at 8% strain in (100) W, whereas Schneider et al. (2009) report a value of 0.21 at 5% strain. Our data range is comparable with reported literature. Such strain rate dependent power law exponent illustrates that size effect exponent is not an intrinsic parameter to the materials, which agree with the previous finding that the size effect exponent is sensitive to the initial structure and density of dislocations in the materials (Gu and Ngan, 2013).

3.2. Strain rate dependence of the strain hardening rate (SHR)

The strain hardening rate (SHR) is calculated as the slope of the true stress–strain curve between 5% and 15% strain. This definition of SHR is similar to other studies of nanopillar compressions (Frick et al., 2008; Volkert and Lilleodden, 2006). According

[1] In the literature (Brinckmann et al., 2008; Abad et al., 2016), σ_0 has been taken as 0 while calculating the power law exponent α from the loglog plot of σ_y vs. d.

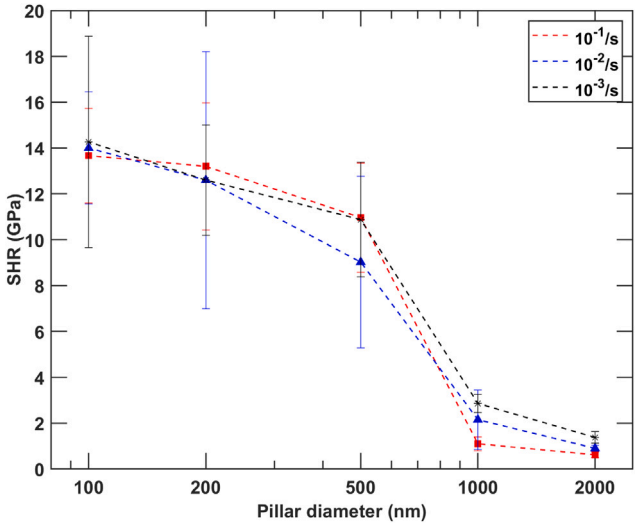

Fig. 5. Plot of the strain hardening rate (SHR) as a function of the pillar diameter (log scale) at different strain rates.

to the engineering stress-engineering strain curves shown in Fig. 2, the SHR is expected to increase with decreasing pillar diameter, which is consistent with previous studies on both fcc and bcc small size metals (Volkert and Lilleodden, 2006; Schneider et al., 2011). This trend is quantitatively demonstrated in Fig. 5, which shows clear size dependence but weak strain rate dependence for 1000 nm and 2000 nm pillars, whereas for 100, 200 and 500 nm pillars there is no clear trend of the SHR at different strain rates. These results of size dependent SHR are similar to those reported by Abad et al. (2016) for W pillars at 25 °C and 10^{-3} s^{-1} strain rate.[2]

The general trend of the size dependence of SHR can be understood as follows. The small scaled plasticity is controlled by the activation of limited amount of dislocation sources. The weak dislocation sources operate firstly and contribute to a specific amount of plastic strain. After these sources are broken or interact with other dislocations, stronger dislocation sources have to be activated to carry the plastic deformation, which implies an increase of the flow stress. Therefore, the strain hardening is because of the exhaustion of weak dislocation sources in smaller pillars leading to the requirement of higher stresses to activate new dislocation sources. Due to the existence of a very limited number of dislocation sources in small pillars, appreciable scatter of the data are observed in small pillars. This depends on initial concentration of dislocation sources which may be influenced by the ion damage caused by FIB milling process and can cause considerable scattering as is the case for 100, 200 and 500 nm pillars. The smaller the sample size, the more appreciable scatter the dislocation source strength, and therefore the higher the SHR. Such effect is much stronger than the influence of the strain rate, so no clear trend of strain rate dependence of SHR is observed. When the pillar size is equal to or larger than 1000 nm, weak strain rate dependence of SHR emerges. For such larger sample, the yield strength also shows clear strain rate dependence. The higher the strain rate, the higher the yield strength, the larger amount the activated dislocation sources. Therefore, the flow stress does not need to increase too much to operate dislocation sources, which suggests relatively lower SHR.

4. Spatio-temporal intermittent plasticity

We discuss here the deformation morphology of compressed pillars. Observations of shape change during plastic deformation will be used to determine the extent of deformation localization and the spatial plastic instability. We will then discuss in this section the size tuned strain rate dependence of strain bursts, as such bursts reflect the extent of the temporal plastic instability.

4.1. Spatial scale: deformation morphology

Fig. 6 shows post compression SEM images of representative W pillars as a function of pillar diameter and strain rate. These pillars were compressed to a strain of 20% to 25%. 2000 nm pillars show relative homogeneous deformation for all strain rates. The deformation morphology does not show significant strain rate dependence. For smaller pillars, 500 and 200 nm, the deformation is more localized at low strain rates and more homogeneous at high strain rates. At low strain rate, the deformation mainly occurs at the top and bottom region, while at high strain rate, more slip traces are also observed in the middle region of the pillar. This is consistent with our recent dislocation dynamics simulation results on the strain rate effect of the deformation behavior of W (Cui et al., 2019).

[2] Our absolute values of SHR are lower than their data, because they used engineering stress and strain data to calculate SHR.

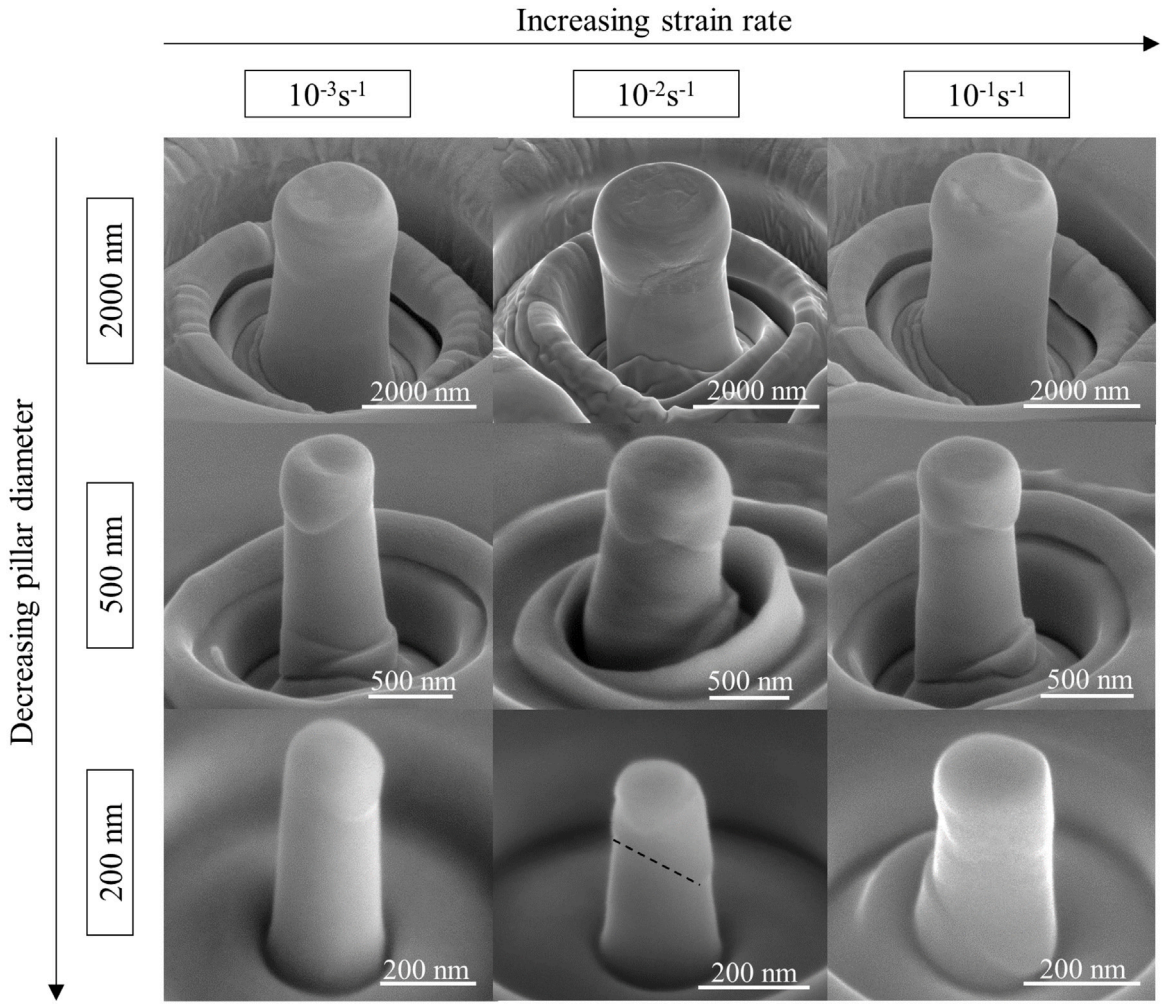

Fig. 6. SEM images of representative post compression W pillars of diameters 2000, 500 and 200 nm, compressed at applied strain rates of $10^{-3}, 10^{-2}$ and 10^{-1} s^{-1}. The dotted line in 200 nm pillar indicates the trace of a slip band.

Recent work done by Song et al. (2019) also supports the idea that higher strain rates correspond to less localization. Sparks et al. (2019) found a clear trend of increasing delocalization with increasing strain rate in compressed Nb pillar, even when the pillar diameter reaches 2000 nm. Compared with the slip-line morphology shown in Nb pillars (bcc) (Sparks et al., 2019) and Ni pillars (fcc) (Dimiduk et al., 2005), the deformation localization extent in our W pillars is weaker.

In the current work, we chose the pillar with conventional cylindrical shape, which is widely used in most of the micropillar compression tests. This makes it be easy to compare with the available experimental results. Note that it has been recently argued that the localized deformation may be related with the cylindrical shape of the pillar which can induce stress concentrations at the top surface. Xu et al. (2020) investigated two types of pillars with conventional cylindrical shape or dog-bone shape under compression, at size scale > 2000 nm. They found that most of slip bands are initiated from the top region of the conventional cylindrical micropillars, whereas for dog-bone micropillars, slip bands begin at the gauge region and continuous slips happen. This work may lead to new ideas to eliminate the effect of stress concentration at the top surface of cylindrical pillars on the deformation morphology. However, some local deformation features are still observed in their deformed dog-bone micropillars (such as Fig. 8 in Xu et al. (2020)). The size dependent deformation localization has been widely observed (Greer, 2006; Dimiduk et al., 2005; Lin et al., 2016). Even loaded in a high-symmetry orientation, a transition from multiple slip to single slip with decreasing sample size is still observed during the pillar compression tests. This is attributed to the discreteness of dislocation source distribution, which leads to the deformation localization at small scale, instead of significant dislocation multiplication and tangles in larger sample (Kiener et al., 2011). Dedicated investigations will further reveal how pillar geometry influences the extent of deformation localization at smaller scales (<2000 nm).

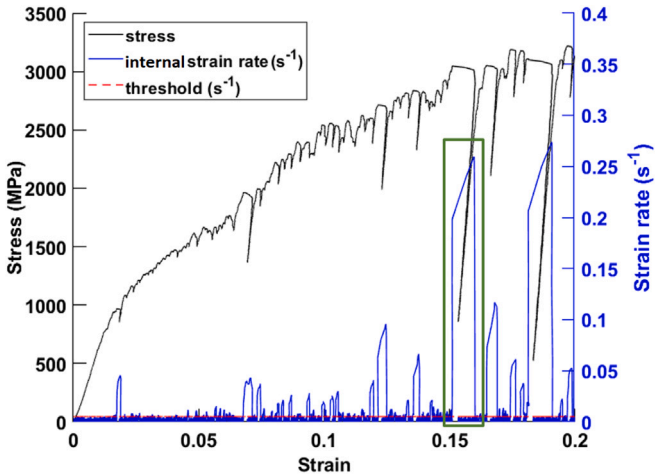

Fig. 7. Evolution of the stress and internal strain rate during compression of a representative 500 nm pillar at an applied strain rate of 10^{-3} s^{-1}.

Table 2
Parameter details for fitting truncated power law functions for burst size PDF of each pillar at various strain rates.

Pillar diameter	Displacement rate	Threshold, v_{thr}	S_{min}	Power law exponent, α	Truncation factor, λ
	300 nm/s	400 nm/s		1.34	6.33×10^{-3}
1000 nm	30 nm/s	40 nm/s	0.5 nm	1.42	4.47×10^{-2}
	3 nm/s	4 nm/s		1.64	2.44×10^{-1}
	150 nm/s	180 nm/s			
500 nm	15 nm/s	18 nm/s	0.5 nm	1.43	3.34×10^{-2}
	1.5 nm/s	3 nm/s			
	60 nm/s	120 nm/s			
200 nm	6 nm/s	15 nm/s	0.5 nm	1.53	4.33×10^{-2}
	0.6 nm/s	2 nm/s			

4.2. Temporal scale: burst statistics

As evident from Figs. 2 and 7, unlike bulk single crystals with smooth stress–strain curves, smaller pillars exhibit an initial elastic region followed by an intermittent plastic region of discrete strain bursts. These plastic strain instabilities are attributed to rapid movement of dislocations when the internal strain rate becomes higher than the applied strain rate (Cui et al., 2019). Therefore, it is expected that the strain rate will influence the observation of strain bursts.

In the following, we will first discuss the detailed method of distinguishing strain bursts from experimental data, and then address the question of burst statistics. Burst events were identified using the raw displacement time data $d(t)$ obtained from the Hysitron PI 85L PicoIndenter. This raw displacement–time evolution data are first smoothed using a low-pass filter to remove the high frequency noise, such as shown in Fig. 8a. The smoothed data is shifted in time to account for the filter delay and then differentiated using a MATLAB moving window function (John D'Errico, Mathworks File Exchange) to get a velocity time profile $v(t)$ of the top surface of the pillar during compression (see Fig. 8b). A strain burst event starting at time t_{start} and ending at time t_{end} is defined as (Dimiduk et al., 2007; Friedman et al., 2012; Uhl et al., 2015),

$$\begin{aligned} v(t_{start}) = v(t_{end}) = v_{thr}. \\ v(t) > v_{thr}, \text{ for } t_{start} < t < t_{end} \end{aligned} \tag{3}$$

where v_{thr} is the threshold value of the displacement rate, which is related to the displacement rate of the compressor tip and is set higher than the displacement rate noise of individual experiments, as listed in Table 2. The internal strain rate $\dot{\varepsilon}_{internal}$ and the threshold strain rate $\dot{\varepsilon}_{thr}$, shown in Fig. 7, are then calculated as

$$\dot{\varepsilon}_{internal} = \frac{v(t)}{h}, \quad \dot{\varepsilon}_{thr} = \frac{v_{thr}}{h} \tag{4}$$

where, h is the initial pillar height.

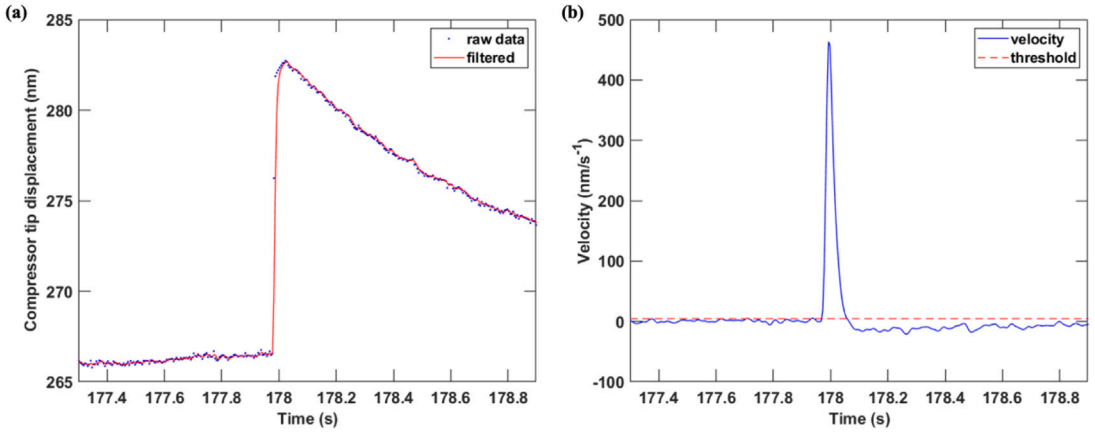

Fig. 8. (a) Displacement–time and (b) velocity–time profiles for a single burst event, which occurred at a strain value of 0.15 (boxed in green) for the 500 nm pillar shown in Fig. 7.

Accordingly, the strain burst size is calculated as,

$$S = d(t_{end}) - d(t_{start}) \tag{5}$$

Here, d and S can be any quantities related to the burst event. For example, if d is the displacement, strain, or time, then S will be displacement burst magnitude, strain burst magnitude, or burst duration. In the following, we will take the burst displacement as an example to analysis the burst statistics. The burst events are evident in the raw displacement signal (Fig. 8a) as jumps in the displacement magnitude located at corresponding start times, t_{start}. The burst event size computed using Eq. (5) was further carefully compared with the jump magnitude obtained from the displacement signal plots to ensure correct estimation of burst events.

We performed statistical analysis of the burst size by calculating the probability density function (PDF) and complementary cumulative distribution function (CCDF). PDF can clearly show whether the strain burst statistics follows the power law scaling, but it needs to introduce some artificial binning size. CCDF does not need to introduce the binning size, and can obtain the maximum resolution of the data without binning size. However, special care should be taken to analyze the power law scaling using CCDF, as discussed in detail in (Friedman et al., 2012; Cui et al., 2017). These results of PDF and CCDF were compared with the mean-field theory (MFT) model predictions about the universal scaling behavior of bursts statistics. MFT model (Friedman et al., 2012) predicts that the probability density function of burst size scales as,

$$P(S) \propto S^{-\kappa} f(S) \tag{6}$$

where S is the burst size, $\kappa = 1.5$, which is the universal critical exponent, and $f(x) \propto e^{-\lambda x}$ is a scaling function to account for the truncation effect. Previous dislocation dynamics simulations (Csikor et al., 2007), force-controlled compression experiments (Brinckmann et al., 2008; Zaiser et al., 2008) and displacement-controlled compression experiments (Maaß et al., 2015; Sparks and Maass, 2018) agree with the universal value of power law exponent, κ. However, the strain rate effect is not carefully investigated in these studies. Our recent DDD simulations (Cui et al., 2017) and displacement-controlled compression experiments (Sparks and Maaß, 2018) have reported strain rate sensitivity of the power law exponent.

Fig. 9 shows PDF and CCDF plots of burst displacement for 1000 nm, 500 nm, and 200 nm pillars at different applied strain rates. More data are shown in the CCDF plot compared with PDF plot, because PDF shows the results with binning, while CCDF can show all the data (Friedman et al., 2012; Cui et al., 2017). A truncated power law (TPL) distribution fit, $P(S) \propto e^{-\lambda S} S^{-\kappa}$ was obtained for each burst size data using the python Power-law package which performs a maximum likelihood estimation of the power law exponent κ and truncation factor λ (Alstott et al., 2014). λ acts as a cutoff for the power law fit of the distribution. In MFT, $P(S)$ follows the power law $S^{-\kappa}$ up to a stress dependent cutoff size, λ^{-1}. These parameters were found to be sensitive to the range of data, S_{min} and S_{max} used for fitting. Increasing the S_{min} increases the value of κ as the power law curve fitting happens on the heavy tail part i.e. the truncated part of the distribution. On the other hand, decreasing the S_{max} excludes the large burst events. Therefore, for uniformity in analysis, the value of S_{min} was chosen based on the standard deviation in displacement signal, measured during noise test of the instrument before each compression session, which was ≤ 0.5 nm. This S_{min} value was fixed for all pillars, and S_{max} was chosen as the largest burst size in each case. In this way, we were able to include all relevant burst events, from the smallest to the largest, for fitting the distribution functions.

Fig. 9 shows different power law exponents at different strain rates for 1000 nm pillars. Table 2 shows all the parameters used and the obtained truncated power law function details for each pillar size at different applied strain rates. The exponents increase in magnitude from 1.34 to 1.64 with decreasing strain rate from 10^{-1} to 10^{-3} s^{-1}, which is consistent with previous experimental (Sparks and Maaß, 2018) and DDD simulation results (Cui et al., 2017; Song et al., 2019). However, for 500 nm and 200 nm pillars, the burst size statistical scaling is insensitive to experimental strain rate, showing exponents of 1.43 and 1.53 respectively at all strain rates, close to the MFT model prediction of 1.5.

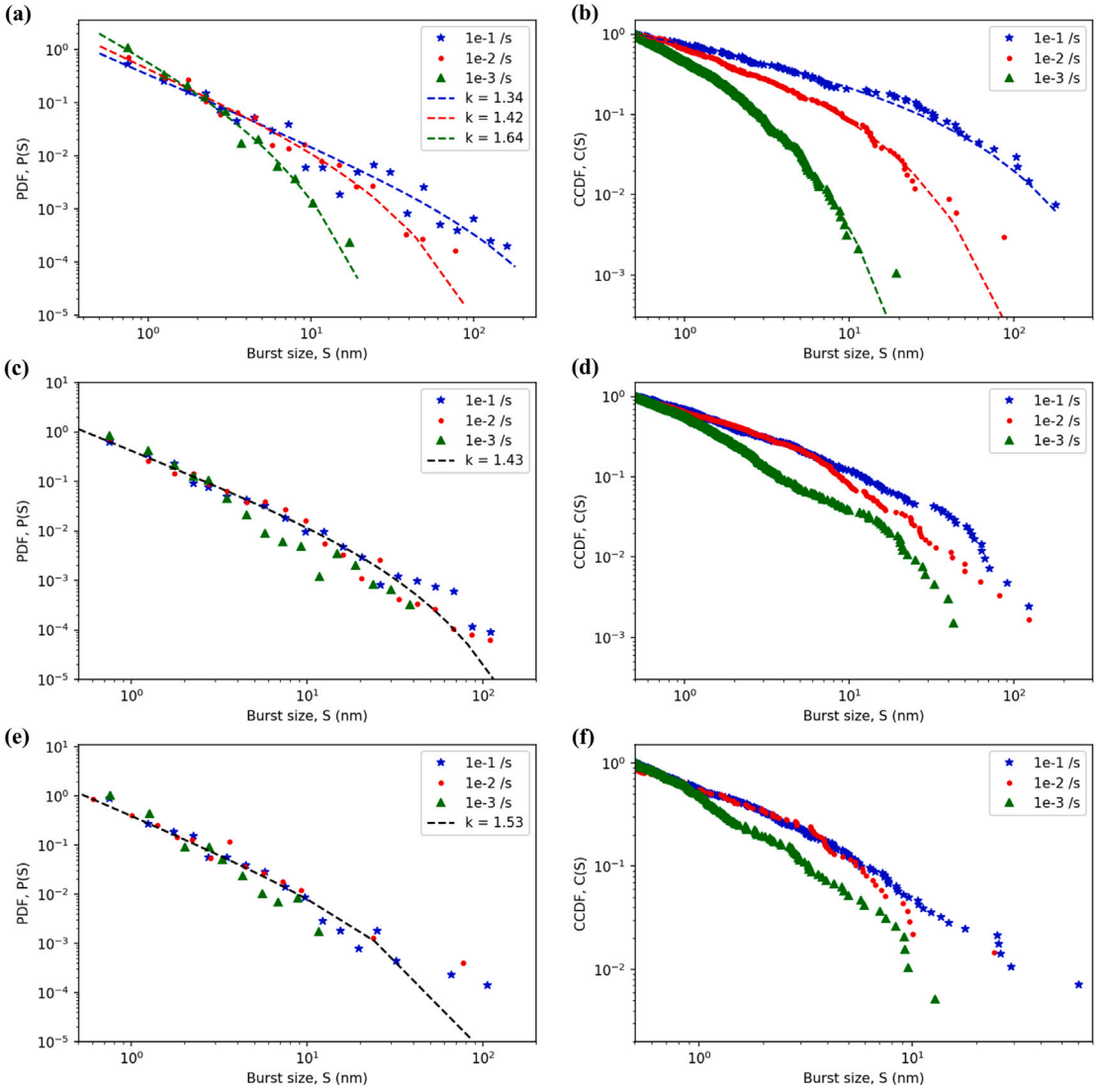

Fig. 9. Statistical analysis of the strain burst size for 1000 nm (a–b), 500 nm (c–d), and 200 nm (e–f) W pillars at applied strain rates of 10^{-3} s^{-1}, 10^{-2} s^{-1}, and 10^{-1} s^{-1}. Figures (a), (c), (e) display the probability density functions (PDFs) and figures (b), (d), (f) display the complementary cumulative distribution functions (CCDFs). Dashed lines in (a), (c) and (e) are the truncated power law fits on the PDF data obtained using the maximum likelihood estimator, where k is the power law exponent. The dashed lines in (b) are gamma functions obtained after integrating the corresponding truncated power law fit function.

5. Combined effect of taper and aspect ratio induced by FIB micromachining

FIB micromachining is a widely used fabrication technique for the majority of the pillar micro-compression studies. It is known to cause geometrical and material complications in the samples (Bei et al., 2007; Zhang et al., 2006; Lee et al., 2016; Schneider et al., 2009; Yilmaz et al., 2019). In the following, the geometrical complications induced by the combined effect of taper and aspect ratio is firstly discussed. Some other aspects of the FIB-related material complications are discussed later in the Appendix.

It is very challenging or may even be impossible to completely remove the taper for FIB fabricated pillars smaller than 1 μm (Frick et al., 2008; Greer and De Hosson, 2011). In the current work, the taper in the pillars was $2.0 \pm 0.5°$ for 2000 nm and 1000 nm diameter, $2.5 \pm 0.5°$ for 500 nm, and $3.5 \pm 0.75°$ for 200 and 100 nm diameters. For pillars of diameters 500, 1000, and 2000 nm, the aspect ratio (length/diameter) was kept around 3. However, for smaller pillars of diameter 100 and 200 nm, this ratio was around 5 because of the difficulty in minimizing the side-wall taper. These ranges of taper and aspect ratio are well within the range of numerous similar-sized pillar compression studies with tapers around $2° - 5°$ and aspect ratio of $3 - 5$ (Frick et al., 2008; Volkert et al., 2006; Greer and De Hosson, 2011; Schneider et al., 2009; Yilmaz et al., 2019).

In the following, the geometrical effects associated with taper and aspect ratio on the measured mechanical response will be analyzed. As shown in Fig. 10(a), the top, middle, and bottom radius of the tapered pillar is r_t, r_m, and r_b, respectively. The aspect

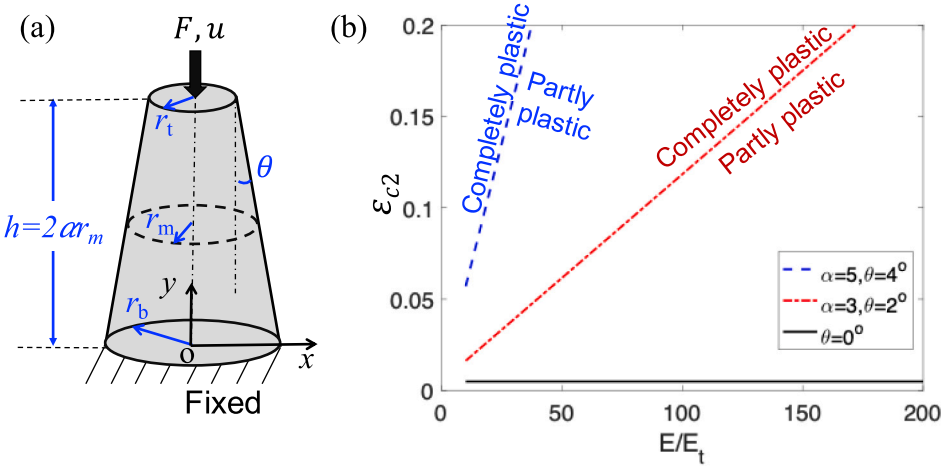

Fig. 10. (a) Schematic showing the considered pillar with taper and key parameters, (b) The critical strain ε_{c2} as a function of the ratio between elastic modulus E and tangent modulus E_t, when the engineering strain ε is higher than ε_{c2}, the pillar completely enters the plastic deformation stage.

ratio $\alpha = h/(2r_m) = h/(r_t + r_b)$, where h is the pillar height, θ is the taper angle, $r_t = r_m(1 - \alpha tan\theta)$, $r_b = r_m(1 + \alpha tan\theta)$. The material parameters are: shear modulus $\mu = 161$ GPa, Poisson's ratio $\nu = 0.28$, elastic modulus $E = 2\mu(1+\nu)$, and a tangent modulus E_t is used to represent the plastic response after reaching the yield stress of the material, σ_{my}. The stress in the horizontal cross section at y is

$$\hat{\sigma}(y) = \frac{F}{\pi(r_b - y tan\theta)^2} \tag{7}$$

where F is the applied force, a superposed $\hat{}$ is used to represent variables corresponding to an infinitely small region centered at a specific horizontal cross section.

If the infinitely small region, corresponding to the horizontal cross section at y, is subjected to elastic deformation, the corresponding strain $\hat{\varepsilon}(y) = \hat{\sigma}(y)/E$, while if it is in plastic deformation, the corresponding strain $\hat{\varepsilon}(y) = \hat{\sigma}(y)/E_t + (1 - E/E_t)\varepsilon_{\text{mp}}$. Here, $\varepsilon_{\text{mp}} = \sigma_{\text{my}}/E$. For the tapered pillar, the plastically deforming zone will propagate down the post axis. The critical position is expressed using y_p, and plastic deformation occurs if $y > y_p$. One can easily find $y_p = (r_b - \sqrt{F/(\sigma_{\text{my}}\pi)})/tan\theta$. Upon integration of strain $\hat{\varepsilon}(y)$ along y, one obtains the displacement u of the top surface,

$$u = \begin{cases} \frac{Fh}{E\pi r_b r_t} & \text{If} \quad F \leqslant \sigma_{\text{my}}\pi r_t^2 \\ \frac{F}{\pi(r_b - y_p tan\theta)}\left(\frac{y_p}{Er_b} + \frac{h-y_p}{E_t r_t}\right) + (1 - \frac{E}{E_t})\frac{\sigma_{\text{my}}}{E}(h - y_p) & \text{If} \quad \sigma_{\text{my}}\pi r_t^2 < F < \sigma_{\text{my}}\pi r_b^2 \\ \frac{Fh}{E_t\pi r_b r_t} + (1 - \frac{E}{E_t})\frac{\sigma_{\text{my}}}{E}h & \text{If} \quad F \geqslant \sigma_{\text{my}}\pi r_b^2 \end{cases} \tag{8}$$

In the experiments, the engineering strain ε is generally calculated as u/h, and the engineering stress σ is calculated by dividing the force with the area of the middle cross section, $\sigma = F/(\pi r_m^2)$. According to Eq. (8), the relation between σ and ε is,

$$\sigma = \begin{cases} \frac{1}{1-p^2}E\varepsilon & \text{If} \quad \varepsilon \leqslant \varepsilon_{c1} \\ \sigma_{\text{my}}\left(\frac{-1+\frac{E}{E_t}+\sqrt{\frac{2}{1/p+1}(1-\frac{E}{E_t})+\frac{2E\varepsilon}{\sigma_{\text{my}}}(\frac{E}{E_t}\frac{1}{1/p-1}-\frac{1}{1/p+1})}}{\frac{E}{E_t}\frac{1}{1-p}-\frac{1}{1+p}}\right)^2 & \text{If} \quad \varepsilon_{c1} < \varepsilon < \varepsilon_{c2} \\ (1-p^2)[\sigma_{\text{my}} + E_t(\varepsilon - \frac{\sigma_{\text{my}}}{E})] & \text{If} \quad \varepsilon \geqslant \varepsilon_{c2} \end{cases} \tag{9}$$

$$p = \alpha tan\theta \tag{10}$$

$$\varepsilon_{c1} = \frac{\sigma_{\text{my}}(1-p)}{E(1+p)} \tag{11}$$

$$\varepsilon_{c2} = \frac{\sigma_{\text{my}}}{E}\left(1 + \frac{E}{E_t}\frac{2}{(\frac{1}{p} - 1)}\right) \tag{12}$$

where p can be considered as a geometrical factor reflecting the combined geometrical effect of taper and aspect ratio on the mechanical response. ε_{c1} and ε_{c2} are critical strains. The pillar with a taper will deform elastically when $\varepsilon \leqslant \varepsilon_{c1}$, and then completely

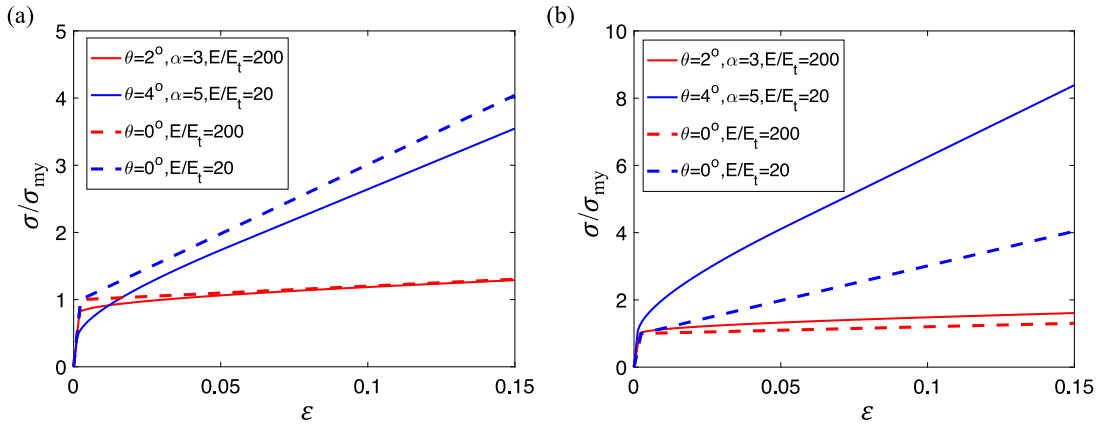

Fig. 11. (a) Engineering strain and engineering stress calculated using the middle cross section area, (b) Engineering strain and engineering stress calculated using the top surface area. θ is taper angle, α is aspect ratio, E is elastic modulus, E_t is tangent modulus, σ_{my} is the material yield stress.

enters the plastic deformation stage only when $\varepsilon \geqslant \varepsilon_{c2}$. It can be found from Eq. (9) that the taper contributes to an increase of the apparent elastic modulus to $1/(1-p^2)$ times the corresponding values without taper during the complete elastic deformation ($\varepsilon \leqslant \varepsilon_{c1}$) , and a decrease of the apparent tangent modulus to $1-p^2$ times the corresponding values without taper during the complete plastic deformation ($\varepsilon \geqslant \varepsilon_{c2}$) regime. For the experimentally considered 100 nm pillar, $\alpha = 5$ and $\theta = 4°$, so $p = 0.35$, $1/(1-p^2) = 1.14$, $1-p^2 = 0.88$. For large samples ($\gtrsim$ 500 nm), $\alpha = 3$ and $\theta = 2°$, so $p = 0.105$, $1/(1-p^2) = 1.01$, $1-p^2 = 0.99$. Therefore, in these two regimes ($\varepsilon \leqslant \varepsilon_{c1}$, and $\varepsilon \geqslant \varepsilon_{c2}$), the error in the calculated stress induced by the taper is within $\sim$ 14% for small pillar, and within $\sim$ 1% for large pillar.

Due to the existence of taper, a significant percentage of the deformation corresponds to the partially plastic deformation regime ($\varepsilon_{c1} < \varepsilon < \varepsilon_{c2}$). Taking $\sigma_{my} = 2$ GPa as an example, the value of ε_{c2} as a function of E/E_t is given in Fig. 10(b). The measured SHR at strain range of 5% $\sim$ 15% in experiments may belong to the partly plastic deformation regime and the complete plastic deformation regime. In the partly plastic deformation regime, the relation between engineering stress and engineering strain is not linear due to taper. The error of the calculated stress in this regime depends on not only the geometrical factor p, but also the modulus ratio E/E_t.

In order to clearly show the effect of taper on the SHR, according to our experiments, two extreme cases are considered: 100 nm pillar with $\theta = 4°$, $\alpha = 5$, $E/E_t \sim 20$, and 2000 nm pillar with $\theta = 2°$, $\alpha = 3$, $E/E_t \sim 200$. The results are compared with the corresponding pillar without taper. It can be observed from Fig. 11(a) that the taper does not significantly change the strain hardening rate. The yield strength for the considered small pillars is underestimated due to the taper by about 12%. Considering the appreciable scatter of the mechanical response in small pillar, this error is acceptable. For the large pillars, much smaller error is observed. Note that in Zhang et al.'s results (Zhang et al., 2006), a much more significant taper effect on SHR is reported. This is possible because in their work, the pillar's top surface area is used to calculate the stress, instead of the middle cross-section area. As shown in Fig. 11(b), if the top area is used, the strain hardening rate is much more sensitive to the taper, compared with Fig. 11(a) where middle cross-section area is used. In addition, higher flow stress is observed in Fig. 11(b) for the pillar with taper, which is consistent with Zhang et al.'s results. The analysis above also shows the importance of using the middle cross-section area of the tapered pillar. In the current work, when the strain rate sensitivity is considered, the effect of taper for the same-sized pillar is similar under different strain rates. Therefore, the taper is expected to have weak influence on the strain rate sensitivity.

6. The competition between size and strain rate effects

The size effect of small-scaled single crystal has attracted attentions for several decades. However, how to take the advantage of size effect to real application is still an open question. The most straightforward way of introducing size effect in large-scaled component is through designing nano-to-micro lattice structures or grain-size engineering (Wei et al., 2006b; Zhang et al., 2019). However, there is limited efforts to investigate the difference between the response associated with the external size and the internal size, and which one is better to be chosen as the degree of design freedom to control the specific mechanical properties of materials. Therefore, it is interesting to compare the size effect in single crystal and polycrystals. Even though there is difference in the deformation mechanism of single crystal and polycrystals, if one ignores the complicated dislocation-grain boundary interaction mechanism and simplifies the grain boundary as impenetrable boundary, each grain can be considered as a coated single crystal, whose coating layer is impenetrable to dislocations. From this point of view, comparing single crystals in terms of polycrystals can be simplified as discussing the coating effect. Most of the previous work focuses on the initial yield behavior and leads to the popular notion that "smaller is stronger". It is of interest then to understand the size effect on the strain rate sensitivity, because the strain rate sensitivity is used as a fingerprint for the thermodynamics and kinetics of plastic deformation (Wei, 2007; Cereceda et al.,

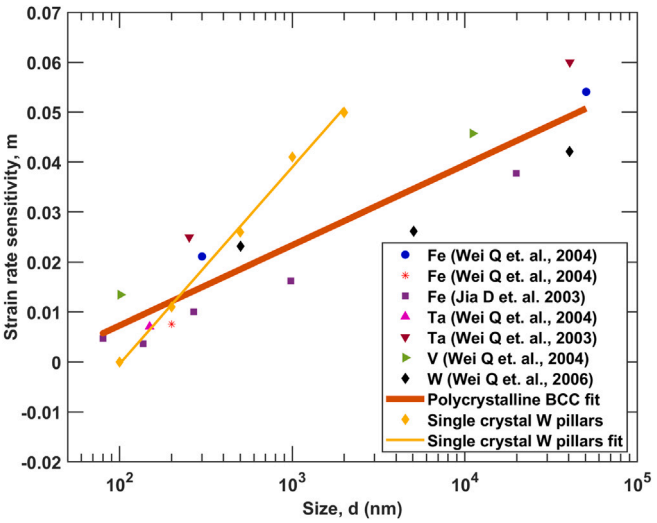

Fig. 12. Strain rate sensitivity parameter, m, for polycrystalline ultra fine grained BCC metals from literature (Wei et al., 2003, 2004, 2006a; Jia et al., 2003) and our single crystal W, as function of d, which is the grain size for polycrystal or sample size for single crystal.

2016), a criterion to assess the possibility of superplastic behavior (Hedworth and Stowell, 1971) and deformation localization (Wei et al., 2006b; Jia et al., 2003).

The experimental observations presented in this work demonstrate that with the reduction of the sample size, the strain rate sensitivity of the flow stress decreases. Similar size dependent strain rate sensitivity is consistent with previous observations in polycrystal W by grain-size engineering (Wei et al., 2006b). Considering that pillar diameters and grain size are typical examples of the external size and internal size, it will be very interesting to compare their roles in influencing the strain rate sensitivity. A quantitative comparison between the effect of sample size and grain size is given in Fig. 12 and Table 3. Note that increasing d in Fig. 12 does not means that it has to be close to the bulk behavior. Because d corresponds to the grain size of a polycrystal or the sample size of a single crystal, higher d means coarser grain or larger single crystal. Therefore, the discussion on the external sample size effect only considers the single crystal, without any grain boundary hardening effect, which is different from the typical bulk sample. Fig. 12 shows that the reduction extent of strain rate sensitivity with decreasing sample size is even more significant in the single crystals by tuning external size, compared with polycrystals with changing grain size.[3]

The difference of the role of the grain size and external size is also manifested by the different trend of strain rate hardening, as shown in Table 3. The SHR decreases with reducing sample size in polycrystal W (Wei et al., 2006b), but increases with reducing external size in W pillars (see Figs. 2 and 5). In ultra fine grained polycrystalline W compression experiments by Wei et al. (2005), flow softening ($SHR < 0$) is observed at higher applied strain rates ($>10^3$ s^{-1}), which implies the occurrence of flow localization. According to Considere–Hart criterion, the propensity of a metal for flow localization under compression α can be estimated as $\alpha = (-SHR/\sigma_y - 1)/m$.[4] Higher α corresponds to greater tendency for flow localization due to the suppression of the stabilizing mechanisms of strain and strain rate hardening. This simple relation implies that the size dependent strain hardening rate, yield stress σ_y, and strain rate sensitivity m all contribute to a more localized deformation for reduced grain size. In our W single-crystal pillars, we also observed more significant flow localization in smaller pillars, but it cannot be well explained by Considere–Hart criterion. In small-scale single crystals, the size dependence of plasticity is generally controlled by the limited number of dislocation sources due to surface annihilation, which is different from the grain boundary effect in polycrystal. Higher SHR values in smaller pillars do not imply more trapped dislocations, as described by the well-known Taylor relation, but is a manifestation of the gradual destruction of weak dislocation sources. We find that the smaller the pillar size, the more scarce are activated dislocation sources, and the more significant is flow localization.

The influence of sample size on the strain rate sensitivity is generally explained based on the following model (Malygin, 2007; Wei et al., 2004). The rate equation for plastic flow controlled by thermal fluctuations is written using an Arrhenius equation (Taylor, 1992),

$$\dot{\gamma} = \dot{\gamma}_0 \exp\left(\frac{-\Delta G(\tau^*)}{k_B T}\right) \tag{13}$$

[3] Note that the strain rate in our experiments ranges from 10^{-3} to 10^{-1}. The experimental data for ultrafine-grained and nanocrystalline bcc metals are obtained at strain rates that range from 10^{-3} to 10^3. Further dedicated efforts may be required to expand the strain rate regime that can be considered during small scale tests.

[4] In other studies, $\alpha = (SHR/\sigma_y - 1)/m$ (Wei et al., 2005). This discrepancy is because we use σ_y to express the absolute value of yield stress, which is described as a negative value under compression in other studies. For compression experiments, the flow will be unstable when $\alpha > 0$. This is possible at high temperature and/or high applied strain rates when there is flow softening, i.e. $SHR < 0$.

Table 3
Size dependent plastic flow of W single crystal pillars and polycrystals. Here, d is sample size or grain size.

	Single crystal pillar	Polycrystal
Strain rate sensitivity m	m $\propto d^{0.67}$	$m \propto d^{0.31}$
Strain hardening rate SHR	Increased SHR for small d	Reduced SHR for small d (Wei et al., 2006b)
Localization	More localized for small d	More localized for small d

where $\dot{\gamma}$ and $\dot{\gamma}_0$ are the shear strain rate and pre-exponential factor involved in the thermal activation, respectively. k_B is Boltzmann constant, T is temperature, ΔG is the activation energy as a function of the shear stress τ^*, which is defined as the applied shear stress minus the athermal internal stress stemming from long-range interactions. The activation volume V is then defined as the derivative of the activation enthalpy with respect to stress (Dora and Rajnak, 1963),

$$V = -\left[\frac{\partial \Delta H(\tau)}{\partial \tau}\right]_T = k_B T\left(\frac{\partial ln\dot{\gamma}}{\partial \tau}\right)_T = k_B T\left(\frac{\partial ln\dot{\gamma}}{\tau \partial ln\tau}\right)_T = \frac{k_B T}{\tau m} \tag{14}$$

Accordingly, $m = k_B T/(\tau V)$. This implies that the strain rate sensitivity is weaker when the applied stress is higher and/or the activation volume is larger. For BCC crystal, the activation volume can be calculated as $V = b^2 l$ (Malygin, 2007). Where b is the Burgers vector magnitude, l is the effective activation distance. At low homologous temperature($T < 0.3T_m$, T_m is melting point), screw dislocations are the dominant carriers of plastic deformation. The motion of the dislocation has to overcome Peierls lattice resistance, the barrier due to the interactions with forest dislocations, and the line tension barrier related to grain boundaries or free surfaces. Accordingly, $l^{-1} = l_p^{-1} + l_g^{-1} + l_f^{-1}$. Here, l_p is associated with the kink-pair mechanism as the critical span between two kinks (Ngan and Wen, 2002), which is only about several tens of Burgers vectors. l_g is related with grain size or sample size d, l_f is associated with dislocation forest interaction mechanism, and is estimated as $1/\sqrt{\rho}$. When d is much larger than l_g (about several nanometers), and ρ is much smaller than about 10^{17} m^{-2}, l is dominated by l_p. This critical span has an inverse square root dependence on applied stress, however, it levels off at very high applied critical stress. This critical stress level can be calculated by the screw dislocation mobility law (Cui et al., 2016b; Po et al., 2016; Cereceda et al., 2016). For screw dislocations, the kink nucleation and motion is of the form

$$v_s = \frac{\tau_{rss} b}{A_s T}\exp\left(-\frac{\Delta G}{k_b T}\right) \tag{15}$$

where, v_s is the screw dislocation velocity, τ_{rss} is the resolved shear stress, b is the Burgers vector magnitude, A_s is the phonon drag constant, T is the test temperature, and ΔG is the Gibbs free energy for the kink pair nucleation. ΔG is given as (Kocks et al., 1975),

$$\begin{aligned} \Delta G &= \Delta H - T\Delta S \\ &= \Delta H_0\left[\left(1 - \left(\frac{\tau^\alpha}{\tau_P}\right)^p\right)^q - \frac{T}{T_c}\right] \end{aligned} \tag{16}$$

where ΔH_0 is the activation enthalpy at zero stress, p and q are two constants reflecting the shape of the Peierls potential, which can be determined by atomistic simulations and experimental data, τ_P is Peierls stress, τ^α is an effective resolved shear stress (rss), which takes non-Schmid effects into account (Gröger et al., 2008; Po et al., 2016; Cereceda et al., 2016). The critical yield stress for W is calculated to be 900 MPa at 298 K, by setting $\Delta G = 0$ in above equations. Since the stress levels obtained in compression experiments for nanocrystalline W and our single crystal W micro and nanopillars are much higher than this critical value, we can conclude that the activation length, l (and hence V) quickly levels off and yield stress, τ becomes the controlling factor for m, where m decreases with increasing τ. This successfully explains the reduced strain rate sensitivity in bcc metals with smaller characteristic lengths.

The comparison of the strain rate sensitivity influenced by grain size and external size can be analyzed as follows. According to the Hall–Patch relation, in polycrystal W, the flow stress $\sigma_y - \sigma_0$ is proportional to $d^{-0.5}$. According to our results shown in Fig. 4, $\sigma_y \propto d^{-0.3}$ in single crystal W pillars. If one only considers the power law term of σ_y with respect to d, the flow stress seems to vary more significantly with respect to grain size, compared with external size. However, the value of σ_0 actually influences the power law exponent, which is not clearly discussed in previous work on polycrystalline W. Thus, based on the power law term alone, the extent of the size dependence of flow stress remains uncertain. Experimental work reported that the flow stresses are 1.5 GPa and 2.5 ~ 3 GPa, when grain sizes are 500 nm and 170 nm, respectively (Kecskes et al., 2007). According to these limited data reported in the literature and compared with our data in Fig. 4, the size dependence of the flow stress in polycrystal W is close to that in single crystal W pillars. Therefore, the effect of flow stress may contribute to similar size dependence of the strain rate sensitivity in polycrystals. In polycrystals, the pile up effect of dislocations around the grain boundary will reduce the mean free path of the dislocation, compared with the free boundary condition in single crystal, so the value of l_g is expected to be smaller in polycrystals. If all other characteristic lengths are the same, the activation volume is expected to be smaller in polycrystals, and the strain rate sensitivity value should be higher. This is consistent with the small size regime (< 200 nm) shown in Fig. 12. However, this model cannot adequately explain the more significant size dependent strain rate sensitivity in single crystals, compared with that in polycrystals, as shown in Fig. 12 for size > 200 nm.

According to our recent dislocation dynamics simulation results (Cui et al., 2016b), with the reduction of the sample size, the role of thermally activated screw dislocation motion gradually decreases. On one hand, the fraction of screw dislocations decreases

sharply with the reduction of sample size due to the inability of small samples to store screw dislocations. Similar lower amount of screw dislocation fraction is also observed in nano-crystalline bcc Mo with the reduction of grain size (Cheng et al., 2013). On the other hand, the very high flow stress in small scale bcc crystals, together with the image force effect, can greatly enhance the mobility of screw dislocations. Therefore, the strain rate sensitivity model on the basis of a single thermally activated process cannot explain the whole story. The relative lower strain rate sensitivity in polycrystals for sizes ranging from about 300 nm to 2000 nm may be because that the strong pile-up effect around the grain boundary on the screw dislocation activities prevails over the effect due to dislocation annihilation from free surface in single crystal for this size regime. This analysis highlights further work that is required for fully understanding the similarity and differences between tuning external and internal sizes.

Going beyond the strain rate sensitivity of the yield stress, our experimental results also demonstrate that the strain rate dependence of dislocation avalanches statistics also become weaker for smaller pillars. This trend is also observed in our recent dislocation dynamics simulations (Cui et al., 2019). For large sample size (such as 1000 nm in Fig. 9), increasing strain rate gradually leads to a reduction of the power law scaling due to an increasingly smaller fraction of small avalanches (Sparks et al., 2019), because a higher strain rate requires more correlated dislocation motion, and some small avalanches may merge at higher strain rates. Through comparing the role of screw dislocation and non-screw dislocations on dislocation avalanches at different strain rates, we find that screw dislocation activities are more important at high strain rates compared with low strain rates (Cui et al., 2019). As the external size gets smaller, it becomes more and more difficult to store many screw dislocations and achieve highly correlated dislocation motion, even at very high strain rates. Therefore, the strain rate effect on dislocation avalanches is gradually overwhelmed by the size effect.

7. Summary and conclusions

In summary, systematic uniaxial in-situ SEM compression experiments were carried out on W micro and nano sized cylindrical pillars. For the first time, we reveal the size effect on the complete picture of the strain-rate-controlled plastic flow behavior in W. We included not only the yield strength, but also the strain hardening rate, and the strain burst statistics. The main finding is that with the reduction of the sample size, the strain rate sensitivity gradually decreases. The critical size of the strain rate insensitivity is around 500 nm for all considered plastic flow behaviors. Such size-tuned strain rate sensitivity is also consistent with our previous finding on the size-tuned temperature sensitivity (Cui et al., 2016b). This external size effect is further compared with the internal grain-size effect with respect to the strain rate sensitivity, strain hardening behavior and flow localization. This leads to the possibility of obtaining better mechanical behavior at corresponding strain rate and temperature conditions by designing the external and internal size of the W component.

Additional conclusions of the present study are:

1. Th flow stress, obtained at 8% strain, exhibits size and strain rate dependence. The power law exponent (α) for size effect decreases with increasing applied strain rate. The strain rate sensitivity parameter (m) decreases with decreasing pillar sizes, implying that the rate of loading has very little effect on the nano size pillars (< 500 nm).
2. The scaling exponent for strain burst statistics are loading rate dependent for micron size pillars (> 1000 nm), where the power law exponent decrease with an increase in the applied loading rate. Nano size pillars (< 500 nm) show near universal power law scaling ($\kappa = 1.50 \pm 0.07$) of strain bursts statistics, independent of the applied loading rate, supporting the observation that nano size pillars are insensitive to strain rates.
3. Micron size W pillars are shown to have homogeneous plastic deformation at all strain rates, whereas nano size pillars exhibit relatively more localized plastic deformation at low strain rates and homogeneous deformation at high strain rates.

CRediT authorship contribution statement

Pratyush Srivastava: Experiments, Formal analysis, Writing - original draft. **Katherine Jiang:** Experiments, Data curation. **Yinan Cui:** Conceptualization, Formal analysis, Writing - original draft, Review. **Edgar Olivera:** Experiments, Validation. **Nasr Ghoniem:** Writing - review & editing, Supervision. **Vijay Gupta:** Writing - review & editing, Supervision.

Declaration of competing interest

The authors declare that they have no known competing financial interests or personal relationships that could have appeared to influence the work reported in this paper.

Acknowledgments

This material is based upon work supported by the National Science Foundation, Grant Numbers CMMI-1024353 and CMMI-1727740 at UCLA. YC acknowledges support from the National Natural Science Foundation of China under Grant No. 11972208 and 11921002.

Appendix

Discussions on other FIB effects

It is well known that FIB milling can introduce surface defects leading to material complication, which can potentially influence the strain hardening rate at the nanometer size scale, due to the Ga layer being deposited on the surface. As the ratio of surface

area to volume increases with smaller sized pillars, the relative scale of the ion irradiated layer increases, causing its effects to become more noticeable. As a result, the dislocation density, due to higher density in the Ga damage layer rather than the single crystal W, also increases. Thus one may be concerned that the higher stress found in smaller pillars is not due to exhaustion of dislocations sources but rather this layer impeding motion of dislocation. However, postmortem images of 100 and 200 nm pillars show clear slip bands ejecting from the pillar, so for the considered case, Ga damage layer is not a strong barrier of dislocation motion. Shan et al. (2008) also demonstrated using *in-situ* TEM compression that dislocations are not impeded by the Ga layer, and many other researchers (Zhang et al., 2014; Kiener and Minor, 2011) report such mechanical annealing (dislocations escaping during compression) as well. Furthermore, the last milling step for ≤ 500 nm sized pillars is performed at $1-10$ pA levels, which help in cleaning the Ga layer away without causing any additional damage.

While it is unlikely that the increased relative size of the damaged layer causes the higher observed stress at small scale by being the load bearing element or causing dislocation pileup (Frick et al., 2008), it is possible that the abundance of dislocation sources from FIB milling lowers the strength required to initiate plasticity (Bei et al., 2007), resulting in the observed size effect in FIB manufactured pillar (von Blanckenhagen et al., 2003). Bei et al. (2007) demonstrated that chemically etched defect-free pillars with no surface damage, in contrast to FIB manufactured pillars, have yield strength independent of sample size close to theoretical strength. This is also observed by Jennings et al. (2010). In addition, pillars created without Ga+ and containing initial dislocations exhibit a size effect akin to those fabricated by FIB (Jennings et al., 2010; Greer et al., 2005). Therefore, size effect is thought to depend on initial, nonzero, dislocation density rather than the manufacturing method. For dislocation-free sample, plasticity is controlled by the dislocation nucleation process, while for the samples with initial dislocations, the plasticity is mainly dominated by the collective behaviors of the dislocations, which is the focus of the current work. Therefore, we did not try to eliminate the initial dislocations, and focused on the study of pillars with initial dislocations.

References

Abad, O.T., Wheeler, J.M., Michler, J., Schneider, A.S., Arzt, E., 2016. Temperature-dependent size effects on the strength of ta and w micropillars. Acta Mater. 103, 483–494.

Alstott, J., Bullmore, E., Plenz, D., 2014. Powerlaw: a python package for analysis of heavy-tailed distributions. PLoS One 9 (1), e85777.

Bei, H., Shim, S., George, E.P., Miller, M.K., Herbert, E., Pharr, G.M., 2007. Compressive strengths of molybdenum alloy micro-pillars prepared using a new technique. Scr. Mater. 57 (5), 397–400.

Bielmann, M., Mahajan, U., Singh, R.K., 1999. Effect of particle size during tungsten chemical mechanical polishing. MRS Online Proc. Libr. Arch. 566.

Brinckmann, S., Kim, J.-Y., Greer, J.R., 2008. Fundamental differences in mechanical behavior between two types of crystals at the nanoscale. Phys. Rev. Lett. 100 (15), 155502.

Butler, B.G., Paramore, J.D., Ligda, J.P., Ren, C., Fang, Z.Z., Middlemas, S.C., Hemker, K.J., 2018. Mechanisms of deformation and ductility in tungsten–a review. Int. J. Refract. Met. Hard Mater. 75, 248–261.

Byer, C.M., Ramesh, K., 2013. Effects of the initial dislocation density on size effects in single-crystal magnesium. Acta Mater. 61 (10), 3808–3818.

Cao, L., Koslowski, M., 2015. Rate-limited plastic deformation in nanocrystalline ni. J. Appl. Phys. 117 (24), 244301.

Cereceda, D., Diehl, M., Roters, F., Raabe, D., Perlado, J.M., Marian, J., 2016. Unraveling the temperature dependence of the yield strength in single-crystal tungsten using atomistically-informed crystal plasticity calculations. Int. J. Plast. 78, 242–265.

Chen, W., Huang, Z., Cao, S., Pan, Y., Huang, M., Hu, Q., Xu, D., Sun, Q., Xiao, L., Sun, J., 2018. Strain rate-induced plasticity in bcc β-ti alloy single crystal micropillars containing brittle ω-precipitates. Mater. Des. 137, 404–413.

Cheng, G., Jian, W., Xu, W., Yuan, H., Millett, P., Zhu, Y., 2013. Grain size effect on deformation mechanisms of nanocrystalline bcc metals. Mater. Res. Lett. 1 (1), 26–31.

Csikor, F.F., Motz, C., Weygand, D., Zaiser, M., Zapperi, S., 2007. Dislocation avalanches, strain bursts, and the problem of plastic forming at the micrometer scale. Science 318 (5848), 251–254.

Cui, Y., Lin, P., Liu, Z., Zhuang, Z., 2014. Theoretical and numerical investigations of single arm dislocation source controlled plastic flow in fcc micropillars. Int. J. Plast. 55, 279–292.

Cui, Y., Po, G., Ghoniem, N., 2016a. Controlling strain bursts and avalanches at the nano-to micrometer scale. Phys. Rev. Lett. 117 (15), 155502.

Cui, Y., Po, G., Ghoniem, N., 2016b. Temperature insensitivity of the flow stress in body-centered cubic micropillar crystals. Acta Mater. 108, 128–137.

Cui, Y., Po, G., Ghoniem, N., 2017. Influence of loading control on strain bursts and dislocation avalanches at the nanometer and micrometer scale. Phys. Rev. B 95 (6), 064103.

Cui, Y., Po, G., Srivastava, P., Jiang, K., Gupta, V., Ghoniem, N., 2019. The role of slow screw dislocations in controlling fast strain avalanche dynamics in body-centered cubic metals. Int. J. Plast..

Dimiduk, D., Uchic, M., Parthasarathy, T., 2005. Size-affected single-slip behavior of pure nickel microcrystals. Acta Mater. 53 (15), 4065–4077.

Dimiduk, D., Uchic, M., Rao, S., Woodward, C., Parthasarathy, T., 2007. Overview of experiments on microcrystal plasticity in fcc-derivative materials: selected challenges for modelling and simulation of plasticitythis paper is from the iutam symposium on plasticity at the micron scale (denmark, 21–25 tmay 2006). Model. Simul. Mater. Sci. Eng. 15 (2), 135, for other papers from this conference see http://www.iop.org/ej/toc/0965-0393/15/1.

Dora, J.E., Rajnak, S., 1963. Nucleation of kink pairs and the peierls'mechanism of plastic deformation.

Dümmer, T., Lasalvia, J., Ravichandran, G., Meyers, M., 1998. Effect of strain rate on plastic flow and failure in polycrystalline tungsten. Acta Mater. 46 (17), 6267–6290.

El Ters, P., Shehadeh, M.A., 2019. Modeling the temperature and high strain rate sensitivity in bcc iron: Atomistically informed multiscale dislocation dynamics simulations. Int. J. Plast. 112, 257–277.

Frick, C., Clark, B., Orso, S., Schneider, A., Arzt, E., 2008. Size effect on strength and strain hardening of small-scale [1 1 1] nickel compression pillars. Mater. Sci. Eng. A 489 (1–2), 319–329.

Friedman, N., Jennings, A.T., Tsekenis, G., Kim, J.-Y., Tao, M., Uhl, J.T., Greer, J.R., Dahmen, K.A., 2012. Statistics of dislocation slip avalanches in nanosized single crystals show tuned critical behavior predicted by a simple mean field model. Phys. Rev. Lett. 109 (9), 095507.

Greer, J.R., 2006. Bridging the gap between computational and experimental length scales: a review on nano-scale plasticity. Rev. Adv. Materialsence 13 (1), 59–70.

Greer, J.R., De Hosson, J.T.M., 2011. Plasticity in small-sized metallic systems: Intrinsic versus extrinsic size effect. Prog. Mater. Sci. 56 (6), 654–724.

Greer, J.R., Oliver, W.C., Nix, W.D., 2005. Size dependence of mechanical properties of gold at the micron scale in the absence of strain gradients. Acta Mater. 53 (6), 1821–1830.

Gröger, R., Bailey, A., Vitek, V., 2008. Multiscale modeling of plastic deformation of molybdenum and tungsten: I. atomistic studies of the core structure and glide of $1/2 < 111 >$ screw dislocations at 0 k. Acta Mater. 56 (19), 5401–5411.
Gu, R., Ngan, A.H.W., 2013. Dislocation arrangement in small crystal volumes determines power-law size dependence of yield strength. J. Mech. Phys. Solids 61 (6), 1531–1542.
Hagen, A., Snartland, B., Thaulow, C., 2017. Temperature and orientation effects on the deformation mechanisms of α-fe micropillars. Acta Mater. 129, 398–407.
Hedworth, J., Stowell, M., 1971. The measurement of strain-rate sensitivity in superplastic alloys. J. Mater. Sci. 6 (8), 1061–1069.
Huang, L., Li, Q.-J., Shan, Z.-W., Li, J., Sun, J., Ma, E., 2011. A new regime for mechanical annealing and strong sample-size strengthening in body centred cubic molybdenum. Nature Commun. 2, 547.
Huang, R., Li, Q.-J., Wang, Z.-J., Huang, L., Li, J., Ma, E., Shan, Z.-W., 2015. Flow stress in submicron bcc iron single crystals: sample-size-dependent strain-rate sensitivity and rate-dependent size strengthening. Mater. Res. Lett. 3 (3), 121–127.
Jennings, A.T., Burek, M.J., Greer, J.R., 2010. Microstructure versus size: mechanical properties of electroplated single crystalline cu nanopillars. Phys. Rev. Lett. 104 (13), 135503.
Jia, D., Ramesh, K., Ma, E., 2003. Effects of nanocrystalline and ultrafine grain sizes on constitutive behavior and shear bands in iron. Acta Mater. 51 (12), 3495–3509.
Jiang, S., Gan, K., Huang, Y., Xue, P., Ning, Z., Sun, J., Ngan, A., 2019. Stochastic deformation and shear transformation zones of the glassy matrix in cuzr-based metallic-glass composites. Int. J. Plast..
Kecskes, L., Cho, K., Dowding, R., Schuster, B., Valiev, R., Wei, Q., 2007. Grain size engineering of bcc refractory metals: Top-down and bottom-up: Application to tungsten. Mater. Sci. Eng. A 467 (1–2), 33–43.
Kiener, D., Guruprasad, P., Keralavarma, S., Dehm, G., Benzerga, A., 2011. Work hardening in micropillar compression: In situ experiments and modeling. Acta Mater. (59), 3825–3840.
Kiener, D., Minor, A., 2011. Source-controlled yield and hardening of cu (1 0 0) studied by in situ transmission electron microscopy. Acta Mater. 59 (4), 1328–1337.
Kim, J.-Y., Jang, D., Greer, J.R., 2009. Insight into the deformation behavior of niobium single crystals under uniaxial compression and tension at the nanoscale. Scr. Mater. 61 (3), 300–303.
Kim, J.-Y., Jang, D., Greer, J.R., 2010. Tensile and compressive behavior of tungsten, molybdenum, tantalum and niobium at the nanoscale. Acta Mater. 58 (7), 2355–2363.
Kocks, U.F., AS, A., MF, A., 1975. Thermodynamics and kinetics of slip.
Lee, S., Jeong, J., Kim, Y., Han, S.M., Kiener, D., Oh, S.H., 2016. Fib-induced dislocations in al submicron pillars: Annihilation by thermal annealing and effects on deformation behavior. Acta Mater. 110, 283–294.
Lin, P., Liu, Z., Zhuang, Z., 2016. Numerical study of the size-dependent deformation morphology in micropillar compressions by a dislocation-based crystal plasticity model. Int. J. Plast. (87), 32–47.
Maass, R., Derlet, P., 2018. Micro-plasticity and recent insights from intermittent and small-scale plasticity. Acta Mater. 143, 338–363.
Maaß, R., Wraith, M., Uhl, J., Greer, J., Dahmen, K., 2015. Slip statistics of dislocation avalanches under different loading modes. Phys. Rev. E 91 (4), 042403.
Malygin, G., 2007. Analysis of the strain-rate sensitivity of flow stresses in nanocrystalline fcc and bcc metals. Phys. Solid State 49 (12), 2266–2273.
Miguel, M.-C., Vespignani, A., Zapperi, S., Weiss, J., Grasso, J.-R., 2001. Intermittent dislocation flow in viscoplastic deformation. Nature 410 (6829), 667.
Ng, K., Ngan, A., 2008. Stochastic nature of plasticity of aluminum micro-pillars. Acta Mater. 56 (8), 1712–1720.
Ngan, A., Wen, M., 2002. Atomistic simulation of energetics of motion of screw dislocations in bcc fe at finite temperatures. Comput. Mater. Sci. 23 (1–4), 139–145.
Ni, X., Zhang, H., Liarte, D.B., McFaul, L.W., Dahmen, K.A., Sethna, J.P., Greer, J.R., 2019. Yield precursor dislocation avalanches in small crystals: the irreversibility transition. Phys. Rev. Lett. 123 (3), 035501.
Papanikolaou, S., Cui, Y., Ghoniem, N., 2017a. Avalanches and plastic flow in crystal plasticity: an overview. Modelling Simulation Mater. Sci. Eng. 26 (1), 013001.
Papanikolaou, S., Dimiduk, D.M., Choi, W., Sethna, J.P., Uchic, M.D., Woodward, C.F., Zapperi, S., 2012. Quasi-periodic events in crystal plasticity and the self-organized avalanche oscillator. Nature 490 (7421), 517.
Papanikolaou, S., Song, H., Van der Giessen, E., 2017b. Obstacles and sources in dislocation dynamics: Strengthening and statistics of abrupt plastic events in nanopillar compression. J. Mech. Phys. Solids 102, 17–29.
Po, G., Cui, Y., Rivera, D., Cereceda, D., Swinburne, T.D., Marian, J., Ghoniem, N., 2016. A phenomenological dislocation mobility law for bcc metals. Acta Mater. 119, 123–135.
Pozuelo, M., Stremfel, J.W., Yang, J.-M., Marian, J., 2019. Strengthening to softening transition in lath martensite. Materialia 5, 100254.
Schneider, A., Frick, C., Clark, B., Gruber, P., Arzt, E., 2011. Influence of orientation on the size effect in bcc pillars with different critical temperatures. Mater. Sci. Eng. A 528 (3), 1540–1547.
Schneider, A., Kaufmann, D., Clark, B., Frick, C., Gruber, P., Mönig, R., Kraft, O., Arzt, E., 2009. Correlation between critical temperature and strength of small-scale bcc pillars. Phys. Rev. Lett. 103 (10), 105501.
Sethna, J.P., Dahmen, K.A., Myers, C.R., 2001. Crackling noise. Nature 410 (6825), 242.
Shan, Z., Mishra, R.K., Asif, S.S., Warren, O.L., Minor, A.M., 2008. Mechanical annealing and source-limited deformation in submicrometre-diameter ni crystals. Nature Mater. 7 (2), 115–119.
Shinzato, S., Wakeda, M., Ogata, S., 2019. An atomistically informed kinetic monte carlo model for predicting solid solution strengthening of body-centered cubic alloys. Int. J. Plast..
Song, H., Dimiduk, D., Papanikolaou, S., 2019. Universality class of nanocrystal plasticity: Localization and self-organization in discrete dislocation dynamics. Phys. Rev. Lett. 122 (17), 178001.
Song, H., Papanikolaou, S., 2019. From statistical correlations to stochasticity and size effects in sub-micron crystal plasticity. Metals 9 (8), 835.
Sparks, G., Cui, Y., Po, G., Rizzardi, Q., Marian, J., Maaß, R., 2019. Avalanche statistics and the intermittent-to-smooth transition in microplasticity. Phys. Rev. Mater. 3 (8), 080601.
Sparks, G., Maaß, R., 2018. Nontrivial scaling exponents of dislocation avalanches in microplasticity. Phys. Rev. Mater. 2 (12), 120601.
Sparks, G., Maass, R., 2018. Shapes and velocity relaxation of dislocation avalanches in au and nb microcrystals. Acta Mater. 152, 86–95.
Taylor, G., 1992. Thermally-activated deformation of bcc metals and alloys. Prog. Mater. Sci. 36, 29–61.
Uchic, M.D., Shade, P.A., Dimiduk, D.M., 2009. Plasticity of micrometer-scale single crystals in compression. Annu. Rev. Mater. Res. 39, 361–386.
Uhl, J.T., Pathak, S., Schorlemmer, D., Liu, X., Swindeman, R., Brinkman, B.A., LeBlanc, M., Tsekenis, G., Friedman, N., Behringer, R., et al., 2015. Universal quake statistics: From compressed nanocrystals to earthquakes. Sci. Rep. 5, 16493.
Volkert, C.A., Lilleodden, E.T., 2006. Size effects in the deformation of sub-micron au columns. Phil. Mag. 86 (33–35), 5567–5579.
Volkert, C., Lilleodden, E., Kramer, D., Weissmüller, J., 2006. Approaching the theoretical strength in nanoporous au. Appl. Phys. Lett. 89 (6), 061920.
von Blanckenhagen, B., Gumbsch, P., Arzt, E., 2003. Dislocation sources and the flow stress of polycrystalline thin metal films. Phil. Mag. Lett. 83 (1), 1–8.
Voyiadjis, G.Z., Song, Y., 2019. Strain gradient continuum plasticity theories: theoretical, numerical and experimental investigations. Int. J. Plast..
Wang, Y., Ma, E., 2004. Strain hardening, strain rate sensitivity, and ductility of nanostructured metals. Mater. Sci. Eng. A 375, 46–52.
Wei, Q., 2007. Strain rate effects in the ultrafine grain and nanocrystalline regimes?influence on some constitutive responses. J. Mater. Sci. 42 (5), 1709–1727.

Wei, Q., Cheng, S., Ramesh, K., Ma, E., 2004. Effect of nanocrystalline and ultrafine grain sizes on the strain rate sensitivity and activation volume: fcc versus bcc metals. Mater. Sci. Eng. A 381 (1–2), 71–79.
Wei, Q., Jiao, T., Mathaudhu, S., Ma, E., Hartwig, K., Ramesh, K., 2003. Microstructure and mechanical properties of tantalum after equal channel angular extrusion (ecae). Mater. Sci. Eng. A 358 (1–2), 266–272.
Wei, Q., Jiao, T., Ramesh, K., Ma, E., Kecskes, L., Magness, L., Dowding, R., Kazykhanov, V., Valiev, R., 2006a. Mechanical behavior and dynamic failure of high-strength ultrafine grained tungsten under uniaxial compression. Acta Mater. 54 (1), 77–87.
Wei, Q., Ramesh, K., Ma, E., Kesckes, L., Dowding, R., Kazykhanov, V., Valiev, R., 2005. Plastic flow localization in bulk tungsten with ultrafine microstructure. Appl. Phys. Lett. 86 (10), 101907.
Wei, Q., Ramesh, K., Schuster, B., Kecskes, L., Dowding, R., 2006b. Nanoengineering opens a new era for tungsten as well. JOM 58 (9), 40–44.
Xu, A., Saleh, M., Davis, J., Edwards, L., Bhattacharyya, D., 2018. In-situ micro-tensile investigation of strain rate response along $< 100 >$ and $< 110 >$ directions in single crystal nickel. Int. J. Plast. 106, 129–144.
Xu, S., Xie, D., Liu, G., Ming, K., Wang, J., 2020. Quantifying the resistance to dislocation glide in single phase fecral alloy. Int. J. Plast. 132, 102770.
Yilmaz, H., Williams, C.J., Risan, J., Derby, B., 2019. The size dependent strength of fe, nb and v micropillars at room and low temperature. Materialia 7, 100424.
Zaiser, M., 2006. Scale invariance in plastic flow of crystalline solids. Adv. Phys. 55 (1–2), 185–245.
Zaiser, M., Schwerdtfeger, J., Schneider, A., Frick, C., Clark, B.G., Gruber, P., Arzt, E., 2008. Strain bursts in plastically deforming molybdenum micro-and nanopillars. Phil. Mag. 88 (30–32), 3861–3874.
Zhang, J., Liang, X., Zhang, P., Wu, K., Liu, G., Sun, J., 2014. Emergence of external size effects in the bulk-scale polycrystal to small-scale single-crystal transition: A maximum in the strength and strain-rate sensitivity of multicrystalline cu micropillars. Acta Mater. 66, 302–316.
Zhang, H., Schuster, B.E., Wei, Q., Ramesh, K.T., 2006. The design of accurate micro-compression experiments. Scr. Mater. 54 (2), 181–186.
Zhang, X., Vyatskikh, A., Gao, H., Greer, J.R., Li, X., 2019. Lightweight, flaw-tolerant, and ultrastrong nanoarchitected carbon. Proc. Natl. Acad. Sci. 116 (14), 6665–6672.